Photonic crystal slabs in flexible organic light-emitting diodes

Arfat Pradana and Martina Gerken*

Institute of Electrical and Information Engineering, Christian-Albrechts-Universität zu Kiel, Kaiserstr. 2, D-24143 Kiel, Germany
**Corresponding author: mge@tf.uni-kiel.de*

Received August 6, 2014; revised November 12, 2014; accepted November 25, 2014; posted January 7, 2015 (Doc. ID 220337); published March 17, 2015

Photonic crystal slabs integrated into organic light-emitting diodes (OLEDs) allow for the extraction of waveguide modes and thus an increase in OLED efficiency. We fabricated linear Bragg gratings with a 460-nm period on flexible polycarbonate substrates using UV nanoimprint lithography. A hybrid organic–inorganic nanoimprint resist is used that serves also as a high refractive index layer. OLEDs composed of a poly(3,4-ethylenedioxythiophene) polystyrene sulfonate (PEDOT:PSS) polymer anode, an organic emission layer [poly(p-phenylene vinylene) (PPV)-derivative "Super Yellow"], and a metal cathode (LiF/Al) are deposited onto the flexible grating substrates. The effects of photonic crystal slab deformation in a flexible OLED are studied in theory and experiment. The substrate deformation is modeled using the finite-element method. The influence of the change in the grating period and the waveguide thickness under bending are investigated. The change in the grating period is found to be the dominant effect. At an emission angle of 20° a change in the resonance wavelength of 1.2% is predicted for a strain of 1.3% perpendicular to the grating grooves. This value is verified experimentally by analyzing electroluminescence and photoluminescence properties of the fabricated grating OLEDs.

OCIS codes: (050.2770) Gratings; (160.5298) Photonic crystals; (230.3670) Light-emitting diodes; (160.4890) Organic materials; (160.5470) Polymers; (250.5230) Photoluminescence.
http://dx.doi.org/10.1364/PRJ.3.000032

1. INTRODUCTION

Organic light-emitting diode (OLED) technology has progressed rapidly over the last decade with OLED flat panel displays already available on the market [1]. As OLEDs may be processed on a variety of substrates they are particularly promising for flexible light-emitting devices that may be rolled up or applied to shaped elements. Flexible top-emitting OLEDs on steel foil have been fabricated [2]. Flexible indium tin oxide (ITO) anodes [3], flexible OLED operation lifetime [4], contrast [5,6], and performance under bending conditions [7] have been studied. Light emission from polymer light-emitting electrochemical cells was demonstrated for strains as large as 120% [8]. In the context of enhanced light extraction efficiency, antireflection nanopillars in flexible OLEDs have been investigated [9]. Periodic nanostructures have been employed for extraction of OLED waveguide modes in standard rigid OLEDs [1,10,11]. They are a means for increasing OLED efficiency as well as for tailoring the angular and spectral emission characteristics. We demonstrated an ITO-free OLED design on a nanostructured substrate employing a polymer anode [12]. We also reported on a composite TiO_2 nanoparticle–polymer nanoimprint resist suitable for nanoimprint lithography [13,14]. We showed waveguide mode extraction for ITO-free OLEDs fabricated on this composite resist material imprinted with a periodic nanostructure [13]. Furthermore, we demonstrated flexible ITO-free OLEDs on polycarbonate substrates with an integrated periodic nanostructure employing the composite TiO_2 nanoparticle–polymer nanoimprint resist [14]. Here, we investigate the effect of the photonic crystal slab deformation in flexible OLEDs in theory and experiment. Figure 1(a) shows a device schematic. Each substrate has four OLEDs on it. Controlled bending of the substrate is achieved using adjustable screws as seen in Fig. 1(b). The effect of device bending is measured in electroluminescence (EL) and photoluminescence (PL) experiments and compared to theoretical predictions.

This paper is structured as follows. Section 2 presents the theory of waveguide mode extraction for deformed photonic crystal slabs on bent substrates. Both the elongation of the grating period and the reduction of the OLED waveguide stack thickness are considered. The theoretically expected resonance emission angle is calculated for an emission wavelength of 550 nm. Section 3 describes the fabrication of the nanostructured flexible OLEDs. Section 4 demonstrates EL of the nanostructured flexible OLEDs and compares the I–V curves with and without bending. In Section 5 PL experiments are presented demonstrating the change in the resonance emission wavelength with deformation. Conclusions are drawn in Section 6.

2. THEORY OF PHOTONIC CRYSTAL SLAB DEFORMATION

The average refractive index of the OLED layer stack is higher than the refractive index of the substrate. Thus, part of the light is emitted into waveguide modes in the OLED layer stack [1]. This light is not emitted to the outside and reduces OLED efficiency. The integration of periodic grating structures (photonic crystal slabs) allows for extracting these waveguide

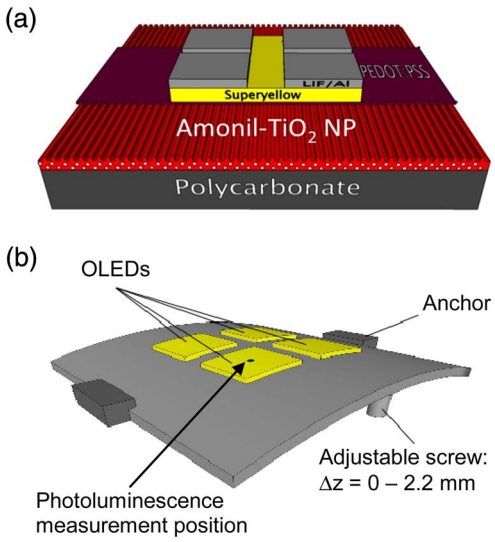

Fig. 1. (a) Schematic diagram of flexible OLED design with periodically nanostructured photonic crystal slab. (b) Controlled substrate deformation employing two screws. Locations of four OLEDs on substrate and PL measurement point are indicated.

modes [1,10–13]. The waveguide mode extraction angle θ depends on the period of the grating structure Λ, the wavelength of light λ, and the mode effective refractive index n_{eff}. θ may be calculated using the Bragg equation given in

$$\sin\theta = n_{\text{eff}} \pm m\frac{\lambda}{\Lambda}, \tag{1}$$

where m is an integer value representing the coupling order. A deformation of the photonic crystal slab will change the grating period Λ and the thickness of the waveguide layers. The thickness change in the waveguide layers causes a change in the mode effective refractive index n_{eff}. Thus, a change in the waveguide mode extraction angle θ is expected at a given wavelength λ for bending of the grating OLED.

As depicted in Fig. 1(b) we employed in the experiments two screws in combination with anchors on two sides of the substrate to realize controlled substrate bending. This bending mechanism has the disadvantage that the strain is nonuniform across the substrate. In order to estimate the position-dependent strain values, finite-element method (FEM) simulations were carried out using the Structural Mechanics Module of COMSOL Multiphysics (COMSOL Inc.). As the OLED layers are thin, they are neglected in the simulation, and only the 1-mm-thick polycarbonate substrate is considered. The Poisson ratio (ν) and the Young's modulus (E) for polycarbonate are set to 0.37 and 2 GPa, respectively.

The bottom edges of the substrate are assumed to be fixed in the y and z directions below the anchors and free to move in the x direction. A prescribed displacement in the z direction, Δz, is enforced at the screw positions. The displacements in the x and y directions are assumed to be zero at the screw positions ($\Delta x = 0$ and $\Delta y = 0$). Figures 2(a)–2(c) show the displacement in the x, y, and z directions calculated for a screw displacement $\Delta z = 2$ mm. All values are normalized to the maximum of the absolute displacement value for the given coordinate. These graphs visualize the inhomogeneous deformation of the OLED substrate under bending. While the x and z displacements mainly change in the x direction, the y displacement also depends on the y direction. In the following a grating vector in the x direction is assumed such that y-direction effects play a minor role. Figure 2(d) plots the strain values in the x direction, ε_x; in the y direction, ε_y; and in the z direction, ε_z, for the screw displacement $\Delta z = 2$ mm for a cut line across two OLEDs. As expected the strain values are strongly position dependent. The values of ε_y and ε_z are nearly identical, indicating that stress values in the y direction are small. The maximum strain is obtained in the center of the substrate with $\varepsilon_x = 1.4\%$ and $\varepsilon_z = -0.50\%$. In the following

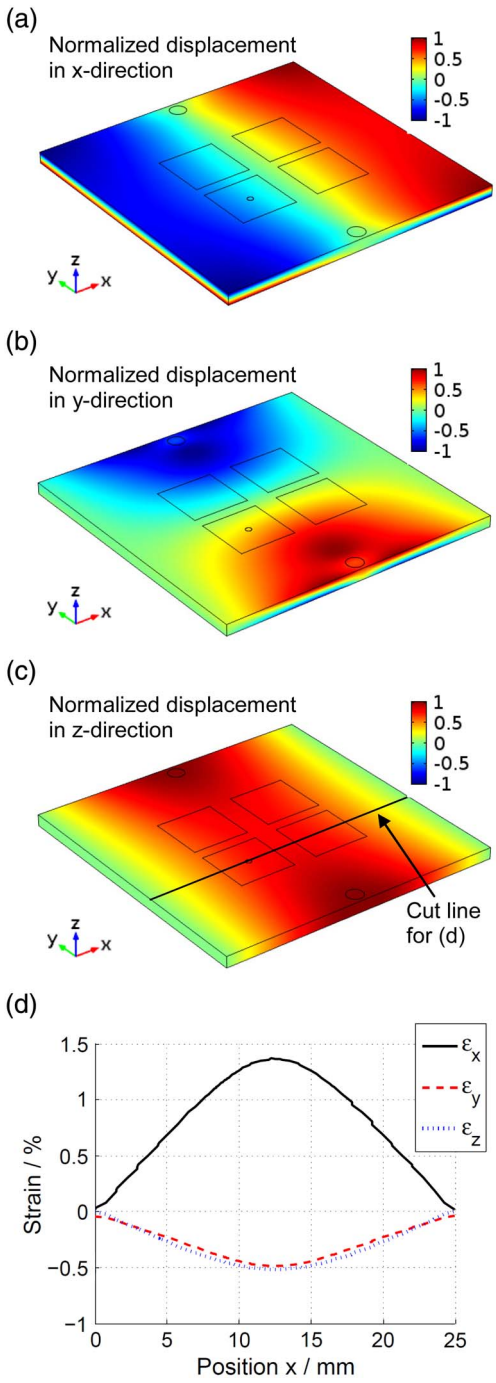

Fig. 2. (a)–(c) FEM simulations of the normalized displacement in x, y, and z directions for a deformation obtained with two screws as depicted in Fig. 1(b). (d) Strain in x, y, and z directions for a screw displacement of $\Delta z = 2$ mm along the surface cut line illustrated in (c).

Table 1. Theoretical Analysis of Strain in x Direction, ε_x, and Compression in y and z Directions, ε_y and ε_z, for Different Screw Displacements Δz in Fig. 1 Calculated Using FEM[a]

Δz (mm)	ε_x (%)	ε_y	ε_z	$-\nu\varepsilon_x$	Λ (nm)	d_{WG} (nm)	TE1:n_{eff} ($\lambda = 550$ nm)	TE1:θ_{th} ($\lambda = 550$ nm)
0	0	0%	0%	0%	460.0	600.0	1.649	26.96°
0.93	0.55	−0.19%	−0.21%	−0.20%	462.5	598.7	1.649	27.38°
1.23	0.72	−0.25%	−0.28%	−0.27%	463.3	598.3	1.648	27.45°
1.505	0.88	−0.31%	−0.34%	−0.33%	464.1	598.0	1.648	27.57°
2.01	1.18	−0.41%	−0.45%	−0.44%	465.4	597.3	1.648	27.79°
2.165	1.27	−0.44%	−0.49%	−0.47%	465.8	597.1	1.648	27.86°

[a]From ε_x the change in the grating period Λ is calculated, and from ε_z the change in the OLED waveguide thickness d_{WG} is calculated. Using the TMM the effective refractive index n_{eff} at $\lambda = 550$ nm is calculated for the TE1 mode. Finally, the theoretically expected resonance emission angle θ_{th} is obtained from the Bragg equation.

the strain values at the dot ($x = 9$ mm, $y = 9.5$ mm) on the lower left OLED are considered. This is also the position of the PL measurements. Here, for $\Delta z = 2$ mm we observe $\varepsilon_x = 1.2\%$ and $\varepsilon_z = -0.45\%$. Table 1 gives the strain values for five different screw displacements Δz calculated for the OLED waveguide at the PL position using FEM simulations. For comparison the calculated values of the Poisson ratio multiplied with ε_x are given. These approximate values of ε_y and ε_z are in agreement with the simulated ones. This demonstrates that the stress values in the y and z directions are negligible at the OLED position for our bending apparatus.

In order to predict the change in the Bragg emission angle θ (compared to the local surface normal), the change in the Bragg grating period and the mode effective refractive index n_{eff} of the waveguide are calculated. It is assumed that the grating period changes proportional to the strain in the x direction, ε_x, as given in

$$\Lambda_{bend} = \Lambda_{flat}(1 + \varepsilon_x). \quad (2)$$

For calculation of the effective refractive index n_{eff} the thicknesses and the refractive indices of the individual layers in the OLED stack need to be considered. Here, simulations are carried out for a wavelength of 550 nm, and the values given in Table 2 are employed. Under bending all layer thicknesses are assumed to be compressed by the strain ε_z obtained from the FEM simulation as given in

$$d_{bend} = d_{flat}(1 + \varepsilon_z). \quad (3)$$

The refractive index values are assumed to be unchanged under bending. Carrying our transfer matrix method (TMM) simulations, the effective refractive index n_{eff} is obtained for the different modes. Table 1 lists the period Λ, total OLED waveguide thickness d_{WG}, and effective refractive index n_{eff} for the TE1 mode under different bending conditions. From these values the theoretically expected resonance emission angle θ_{th} is calculated using the Bragg equation. For a screw displacement of up to $\Delta z = 2.2$ mm only a small change in the Bragg emission angle of approximately 1° is predicted. In the following we will compare this prediction to experimental results.

Table 2. Layer Thicknesses and Refractive Indices at a Wavelength of 550 nm Used in the Transfer Matrix Simulations for Determining the Effective Refractive Index n_{eff} [14]

Material	Thickness (nm)	$n_{550\,nm}$
Polycarbonate		1.59
Amonil-TiO_2	450	1.84
PEDOT	70	1.59
Super yellow	80	1.9
Aluminum		1.0 + i6.4

3. FABRICATION OF FLEXIBLE GRATING OLEDS

OLEDs with an integrated photonic crystal slab are fabricated onto flexible polycarbonate substrates of 25 mm × 25 mm × 1 mm in size [14]. The polycarbonate substrates are cleaned using isopropanol for 15 min. Then the nanoimprint resist is spin-coated onto the substrates. We employ a high-refractive-index composite nanoimprint resist obtained by blending 30% volume TiO_2 nanoparticles dispersed in xylene (purchased from Sigma-Aldrich Co. LLC) into the UV curable resist Amonil (Amonil MMS4 by AMO GmbH, Aachen, Germany) [13]. As a working stamp a polydimethyl–siloxane stamp replicated from a glass master stamp with a 460-nm linear Bragg grating on the surface is utilized [11,13,15]. The linear grating structure is transferred by placing the working stamp on the composite nanoimprint resist layer and by exposition with a dose of 2 J/cm^2 by a UV light source (Beltron GmbH, Rödemark, Germany).

As the photoresist is hydrophobic, the polymer anode material poly(3,4-ethylenedioxythiophene) polystyrene sulfonate (PEDOT:PSS) (aqueous microdispersion Clevios PH500 purchased from Starck GmbH) is mixed with 1% volume of the fluorosurfactant Zonyl FS-300 (purchased from Sigma-Aldrich Co. LLC) to increase the wettability [16]. The mixture is shaken for 1 min and placed in the refrigerator for 24 h. Afterward, the polymer anode mixture solution is deposited using a 0.45 μm polyvinylidene difluoride (PVDF) filter (Carl Roth GmbH, Germany) attached to a syringe. It is spin-coated at a speed of 2000 rpm onto the nanostructured photoresist substrates. The resulting layer is 70 nm thick. The polymer anode mixture is cured by baking in an oven at 80°C for 1 h. For structuring the polymer anode into strip lines, it is partly covered by a stainless steel mask and exposed to an oxygen plasma at 200 W for 3 min. For the transfer the samples are exposed to normal atmosphere. Before deposition of the remaining OLED layers, the polymer anode is baked again at 80°C for 24 h in a glove box under nitrogen atmosphere for dehydration [17].

The organic emission layer PDY-132 [poly(p-phenylene vinylene) (PPV)-derivative “Super Yellow” purchased from Merck OLED Materials GmbH] is spin-coated onto the polymer anode at 2000 rpm in the glove box. The resulting layer thickness is 80 nm. The samples are transferred from the glove

box to the vacuum evaporation chamber under nitrogen atmosphere. As a cathode we deposited 1 nm LiF and 200 nm Al using thermal evaporation. As depicted in Fig. 1, each device has four active areas of 5 mm × 5 mm each.

4. EL RESULTS

The electrical characteristics and the EL of the fabricated devices were evaluated under flat and bent operation. Figure 3(a) presents the current–voltage (I–V) characteristics of the OLEDs measured with a source-measurement unit (Keithley Instruments Inc.). Only small differences in the electrical characteristics are observed. Figure 3(a) also shows a photograph of a device in bent operation. Wavelength- and angle-resolved EL measurements were performed using a goniophotometer setup for sample rotation and bare fiber light collection at a distance of 50 mm. In Figs. 3(b) and 3(c) the EL is shown for a flat substrate and a substrate that is bent by a screw displacement of $\Delta z = 1.48$ mm. The waveguide mode extraction by the grating is clearly visible. From the mode positions a thickness of the composite nanoimprint resist layer of 450 nm is fitted [14]. The calculated extraction angles of the TE0 and the TE1 modes are plotted. Good agreement with the experimental results is observed. From Figs. 3(b) and 3(c) we observe a higher relative intensity of the extracted resonance peaks for bent operation. We have seen this effect throughout our samples, and improved operation under strain has been seen previously in [8]. From the conducted experiments we cannot conclude the reason for this effect.

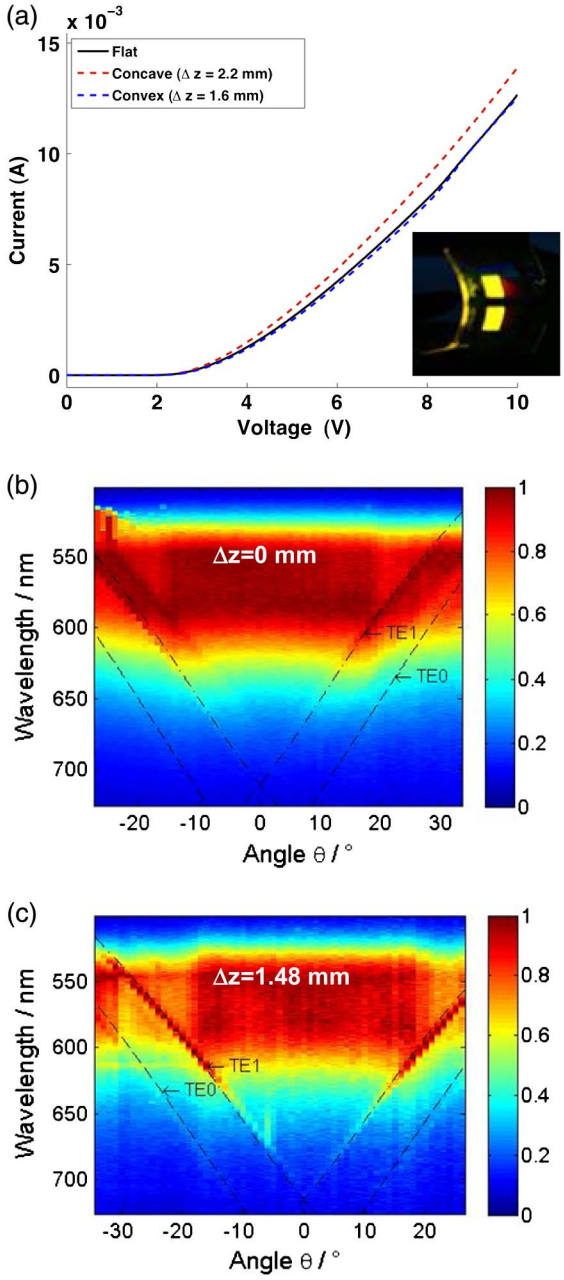

Fig. 3. (a) I–V curve for flat and bent conditions. Inset shows photograph of OLEDs for bending operation. (b) EL characterization of flexible grating OLED with a TE polarization filter. Angle- and wavelength-resolved EL intensity perpendicular to the grating grooves is shown for a flat substrate ($\Delta z = 0$) and a grating period of $\Lambda = 460$ nm. The intensity is normalized to the maximum value at each wavelength. The theoretical extraction angles of the TE0 and TE1 modes are shown for a thickness of the composite nanoimprint resist layer of 450 nm. (c) EL intensity for bent condition obtained by a screw displacement of $\Delta z = 1.48$ mm.

5. PL RESULTS

As discussed in Section 2, the strain is not uniform across the OLED devices for the employed deformation mechanism. Therefore, we performed PL measurements. A UV laser at

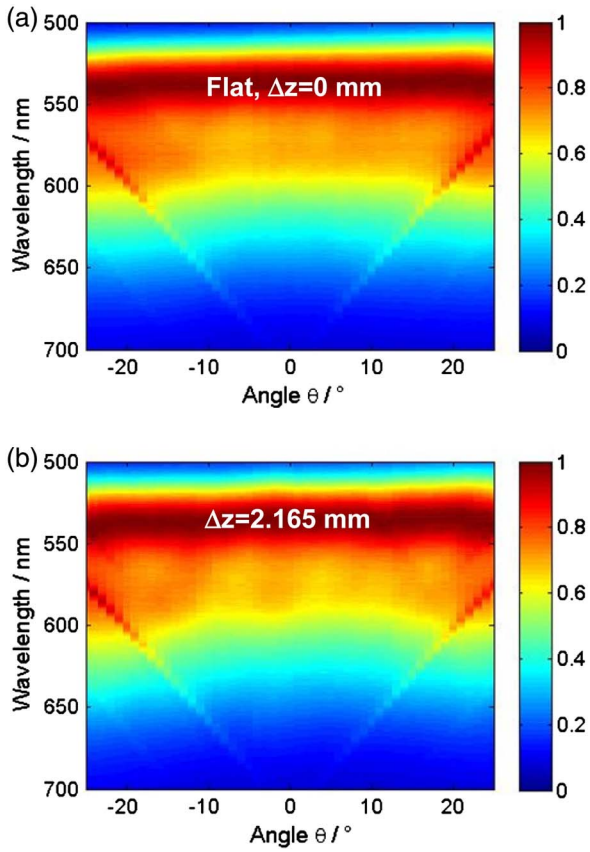

Fig. 4. PL intensity of flexible grating OLED as a function of emission angle and wavelength. The intensity is normalized to the maximum intensity at a given angle. (a) Results for a flat substrate ($\Delta z = 0$) and (b) for bent condition obtained by a screw displacement of $\Delta z = 2.165$ mm. For both strain conditions the grating resonances are clearly visible, and bending causes only a slight shift of the resonances in wavelength.

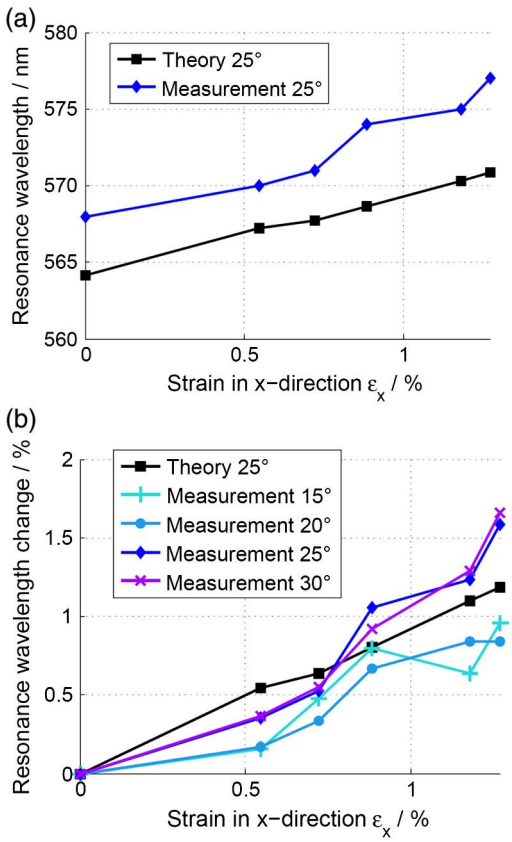

Fig. 5. (a) Resonance wavelength of the TE1 mode at 25° emission angle as a function of the strain in the x direction, ε_x, obtained from screw displacements Δz as given in Table 1. Compared are the experimental value and the theoretical prediction calculated with the Bragg equation, Eq. (1), for the grating periods and the effective refractive indices given in Table 1. (b) Relative resonance wavelength shift under deflection for extraction angles of 15°, 20°, 25°, and 30°.

405 nm excites a small spot on the OLED as depicted in Figs. 1 and 2. The objective of these experiments is to quantitatively compare the effect of photonic crystal slab deformation in experiment and theory. Figure 4 shows two typical examples of PL spectra as a function of angle. Again, the waveguide modes extracted by the grating are clearly visible. In the following we analyze the angle- and wavelength-dependent extraction of the TE1 mode, whose position is indicated in Fig. 3. As the wavelength resolution of the measurements is much better than the angular resolution, we analyze the results considering fixed emission angles. In Fig. 5(a) the resonance wavelength is plotted for a resonance extraction angle of 25°. The theoretical value is calculated assuming a change in the effective refractive index of the mode and the grating period as described in Section 2. Figure 5(b) plots the change in resonance wavelength normalized to the resonance wavelength for a flat substrate. The observed experimental values are in good agreement with the theoretical values. The deviations are within the measurement deviations of the conducted experiments regarding the accuracy in the screw displacement and the extraction of the experimental results from the discrete data set. Thus, the experimental results verify that the theoretical description of the photonic crystal waveguide deformation presented in Section 2 is suitable for analyzing the behavior of the fabricated flexible grating OLEDs.

6. CONCLUSIONS

We investigated the influence of the deformation of a photonic crystal slab integrated into a flexible OLED in theory and experiment. Theory and experiment show an agreement that relatively small spectral changes occur under bending. A model based on calculating the strain-dependent grating period and layer thicknesses delivers good predictions. In conclusion, photonic crystal slabs may be integrated into bendable OLEDs for improved extraction efficiency without much adverse influence on extraction properties due to the relatively small strain values under bending. For stretchable OLEDs, on the other hand, our results suggest that large strain values will be accompanied by significant spectral changes.

ACKNOWLEDGMENTS

We acknowledge support by the Bundesministerium für Bildung und Forschung (BMBF) within the project NanoFutur under Project No. 03X5514.

REFERENCES

1. A. Buckley, ed., *Organic Light-Emitting Diodes (OLEDs), Materials, Devices and Applications* (Woodhead, 2013).
2. Z. Xie, L.-S. Hung, and F. Zhu, "A flexible top-emitting organic light-emitting diode on steel foil," Chem. Phys. Lett. **381**, 691–696 (2003).
3. J. Zhao, S. Xie, S. Han, Z. Yang, L. Ye, and T. Yang, "A bilayer organic light-emitting diode using flexible ITO anode," Phys. Status Solidi **184**, 233–238 (2001).
4. M. S. Weaver, L. A. Michalski, K. Rajan, M. A. Rothman, J. A. Silvernail, J. J. Brown, P. E. Burrows, G. L. Graff, M. E. Gross, P. M. Martin, M. Hall, E. Mast, C. Bonham, W. Bennett, and M. Zumhoff, "Organic light-emitting devices with extended operating lifetimes on plastic substrates," Appl. Phys. Lett. **81**, 2929–2931 (2002).
5. A. N. Krasnov, "High-contrast organic light-emitting diodes on flexible substrates," Appl. Phys. Lett. **80**, 3853–3855 (2002).
6. S.-Y. Kim, J.-H. Lee, J.-H. Lee, and J.-J. Kim, "High contrast flexible organic light emitting diodes under ambient light without sacrificing luminous efficiency," Org. Electron. **13**, 826–832 (2012).
7. R. Paetzold, K. Heuser, D. Henseler, S. Roeger, and G. Wittmann, "Performance of flexible polymeric light-emitting diodes under bending conditions," Appl. Phys. Lett. **82**, 3342–3344 (2003).
8. J. Liang, L. Li, X. Niu, Z. Yu, and Q. Pei, "Elastomeric polymer light-emitting devices and displays," Nat. Photonics **7**, 817–824 (2013).
9. Y.-H. Ho, C.-C. Liu, S.-W. Liu, H. Liang, C.-W. Chu, and P.-K. Wei, "Efficiency enhancement of flexible organic light-emitting devices by using antireflection nanopilars," Opt. Express **19**, A295–A302 (2011).
10. J. M. Lupton, B. J. Matterson, I. D. W. Samuel, M. J. Jory, and W. L. Barnes, "Bragg scattering from periodically microstructured light emitting diodes," Appl. Phys. Lett. **77**, 3340–3342 (2000).
11. U. Geyer, J. Hauss, B. Riedel, S. Gleiss, U. Lemmer, and M. Gerken, "Large-scale patterning of indium tin oxide electrodes for guided mode extraction from organic light-emitting diodes," J. Appl. Phys. **104**, 093111 (2008).
12. B. Riedel, J. Hauss, U. Geyer, J. Guetlein, U. Lemmer, and M. Gerken, "Enhancing outcoupling efficiency of indium-tin-oxide-free organic light-emitting diodes via nanostructured high index layers," Appl. Phys. Lett. **96**, 243302 (2010).
13. A. Pradana, C. Kluge, and M. Gerken, "Tailoring the refractive index of nanoimprint resist by blending with TiO_2 nanoparticles," Opt. Mater. Express **4**, 329–337 (2014).
14. A. Pradana and M. Gerken, "Nanostructured, ITO-free electrodes for OLED emission control," in *MRS Proceedings*, Vol. **1699** (Cambridge University, 2014).
15. M. Hansen, M. Ziegler, H. Kohlstedt, A. Pradana, M. Rädler, and M. Gerken, "UV capillary force lithography for multiscale structures," J. Vac. Sci. Technol. B **30**, 031601 (2012).

16. M. Vosgueritchian, D. J. Lipomi, and Z. Bao, "Highly conductive and transparent PEDOT:PSS films with a fluorosurfactant for stretchable and flexible transparent electrodes," Adv. Funct. Mater. **22**, 421–428 (2012).

17. A. M. Nardes, M. Kemerink, M. M. de Kok, E. Vinken, K. Maturova, and R. A. J. Janssen, "Conductivity, work function, and environmental stability of PEDOT:PSS thin films treated with sorbitol.," Org. Electron. **9**, 727–734 (2008).